



# The orientation and optical properties of inverted-pyramid-like structures on multi-crystalline silicon textured by Cu-assisted chemical etching

Juntao Wu<sup>a,b</sup>, Yaoping Liu<sup>a,\*</sup>, Quansheng Chen<sup>a,b</sup>, Wei Chen<sup>a,b</sup>, Lixia Yang<sup>a</sup>, Yan Wang<sup>a</sup>, Meiliang He<sup>c</sup>, Xiaolong Du<sup>a,b,\*</sup>

<sup>a</sup> Key Laboratory for Renewable Energy, Beijing Key Laboratory for New Energy Materials and Devices, National Laboratory for Condensed Matter Physics, Institute of Physics, Chinese Academy of Sciences, Beijing 100190, China

<sup>b</sup> University of Chinese Academy of Sciences, Beijing 100049, China

<sup>c</sup> Baoding Lightway Green Energy Technology Co., Ltd., 071000, China

## ARTICLE INFO

### Keywords:

Cu-assisted chemical etching  
Diamond wire sawn  
Inverted pyramid  
Grain orientation  
Multi-crystalline silicon

## ABSTRACT

An effective low-cost texturing method based on the Cu-assisted chemical etching (CACE) technique was adopted to thoroughly texture diamond wire sawn (DWS) multi-crystalline silicon (mc-Si) wafers to form inverted-pyramid-like (IPL) structures on different grains. A mathematical model was first established to confirm the orientation of the IPL structures on grains  $\langle 110 \rangle$ , grains  $\langle 112 \rangle$  and grains  $\langle 113 \rangle$ ; this confirmation enables one to deeply understand the CACE process for mc-Si. In addition, the optical properties of IPL structures on different grains were investigated. We reveal that the IPL texture reduces the wafer reflectance to a much lower level of 22.4% and 4.4% before and after SiNx deposition, respectively. Due to the lower reflectance, the average cell efficiency for IPL textured wafers is as high as 19.03%, which is 0.52% absolute higher than that for wafers textured using HF/HNO<sub>3</sub> mixture solutions. This CACE technique paves new insight to promote the industrial application of DWS mc-Si solar cells.

## 1. Introduction

Crystalline silicon solar cells account for the largest share of today's solar cell market and will maintain this tendency for the next ten years (Macdonald et al., 2004). Since 60% of the cost of solar cells is the wafer material, the use of mc-Si, which has a 30–50% lower cost compared to mono-crystalline silicon and shares more than half a percent of the market, is therefore the subject of increasing interest for the future solar energy market (Kumagai, 2015; Möller et al., 2005). To further suppress the cost and promote the development of the photovoltaic market, novel technologies must be introduced for cutting the silicon ingots into wafers to solve the disadvantages of the slurry wire-sawing (SWS) method such as slow cut speed, waste generation and high breakage of steel-wire, etc. (Watanabe, et al., 2010; Meinel et al., 2012). Hence, some research groups have studied a new slicing method (Möller et al., 2011; Wu et al., 2001; Chung and Nhat, 2014), called the diamond wire sawn (DWS) technique, which has become an alternate to the SWS method (Möller, 2004, 2006; Bhagavat et al., 2000; Yu et al., 2012); the new DWS technology successfully settles the high-cost problem, providing many advantages, such as a higher productivity, an

easier recycling of the cooling liquid, and a lower wear of the wire (Bidiville et al., 2009; Yang et al., 2013; Meng and Zhou, 2014). Meanwhile, research groups have demonstrated that DWS wafers show more than a factor of two smaller saw-damage-layer thicknesses compared to that of SWS wafers (Watanabe et al., 2010); this outcome is suitable for the fabrication of solar cells, particularly thin silicon cells where the wafer thicknesses approach or become less than 150 μm (Chen et al., 2015). The surface of the wafers produced by DWS is different from that produced by SWS. The damage layer is distributed homogeneously on SWS wafers. Raman analysis of the wafer surface shows that only crystalline silicon is present on the surface (Bidiville et al., 2009). Thus, shallow pits in the micrometer range can be formed by using the conventional texturing of isotropic etching with HF/HNO<sub>3</sub> acid solutions. An amorphous layer of silicon, however, was found on the surface of DWS wafers (Chen et al., 2015), which can act as an efficient mask during etching because the amorphous silicon has an etching rate that is approximately 30 times slower than that for crystalline silicon along the  $\langle 100 \rangle$  direction (Kawasegi et al., 2005). Thus, the conventional acid texturing method does not work well on DWS mc-Si wafers and currently hinders further development of this innovative

\* Corresponding authors at: Key Laboratory for Renewable Energy, Beijing Key Laboratory for New Energy Materials and Devices, National Laboratory for Condensed Matter Physics, Institute of Physics, Chinese Academy of Sciences, Beijing 100190, China (X. Du).

E-mail addresses: [ypliu@iphy.ac.cn](mailto:ypliu@iphy.ac.cn) (Y. Liu), [xldu@iphy.ac.cn](mailto:xldu@iphy.ac.cn) (X. Du).

<https://doi.org/10.1016/j.solener.2018.07.011>

Received 25 May 2018; Received in revised form 3 July 2018; Accepted 5 July 2018

0038-092X/ © 2018 Elsevier Ltd. All rights reserved.

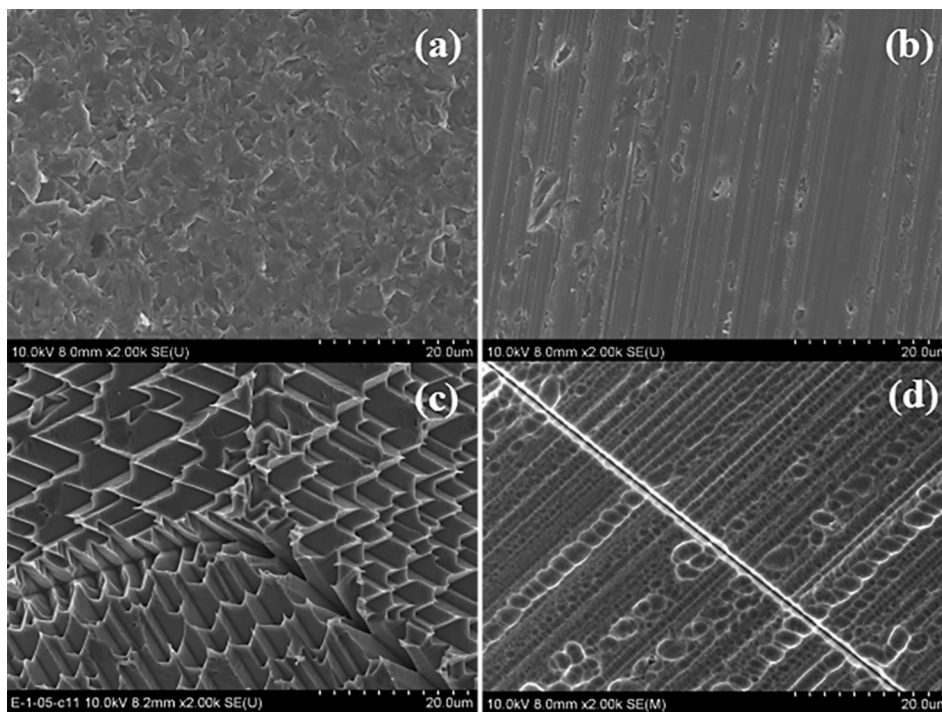


**Fig. 1.** SEM top-view images for mc-Si wafers: (a), (b) as-cut morphologies for SWS and DWS, respectively; (c), (d) textured morphologies for sample A (CACE) and sample B (HF/HNO<sub>3</sub> solutions).

DWS technique (De Wolf et al., 2000; Meinel et al., 2014; Fashina et al., 2015; Lippold et al., 2014).

To solve this texturing difficulty for DWS mc-Si wafers, several groups have put much effort into texturing the DWS mc-Si wafers to reduce the reflectance to an acceptable level. Early on, researchers at AIST in Japan demonstrated that DWS cells with a saw-damage etching depth of 7 µm show photovoltaic properties comparable to cells prepared using SWS wafers and subsequently etched to remove the damage layers up to 15 µm (Watanabe et al., 2010). Subsequently, studies incorporated H<sub>2</sub>SO<sub>4</sub> into the HF/HNO<sub>3</sub> mixture solutions to etch the DWS mc-Si wafers, but the cell efficiency obtained was not satisfactory (Lippold et al., 2014). Additionally, a nanotexture technique was employed to shape pyramidal nanostructures on the surface of DWS mc-Si wafers; unfortunately, this process requires many steps to accomplish, which makes it very complicated and expensive (Cao et al., 2015). In addition, Akira Kumagai adapted a metal catalyst texture using silver nitrate (AgNO<sub>3</sub>) to form a macro-porous Si layer on the surface, with similar deficiencies of high-cost and complexity as well as poor conversion efficiency (Kumagai 2015). As a consequence, an effective texturing method, which is low cost and simple as well as compatible with the current production line must be established to motivate the development of the DWS technique as well as the photovoltaic market.

Inspired by the achievement in texturization of mono-crystalline silicon (Wang et al., 2015), the Cu-assisted chemical etching (CACE) technique was innovatively introduced in this paper to sufficiently texture DWS mc-Si wafers, decreasing the reflectance as well as increasing the cell efficiency. In the present study, the surface property and reflectivity of DWS mc-Si wafers textured by CACE, compared with HF/HNO<sub>3</sub> mixture solutions, have been investigated. Moreover, new models have been put forward to confirm the orientation of the grains and provide deeper insights into understanding the reflectance properties according to the structures formed during the CACE etching. The average cell efficiency for the wafers textured by CACE is 0.52% absolute higher than that for wafers textured using HF/HNO<sub>3</sub> mixture solutions. This technique is low-cost and simple as well as compatible with the current production line, demonstrating huge potential for industrial application.

## 2. Materials and methods

The materials used in this study were boron-doped mc-Si wafers cut using the DWS and SWS techniques, respectively, with a commercial size of 156 mm × 156 mm. The DWS wafers textured by CACE and HF/HNO<sub>3</sub> mixture solutions were labeled sample A and sample B, respectively. The texturing of sample A was carried out in a polytetrafluoroethylene container, which was filled with 0.005 M Cu(NO<sub>3</sub>)<sub>2</sub>, 4.6 M HF and 0.55 M H<sub>2</sub>O<sub>2</sub> for 15 min at 50 °C; the details have been discussed in our previous work (Wang et al., 2015). The sample B was textured by using the current production line method. Before texturization, the Si wafers were cleaned by acetone, ethanol, and deionized water (DIW) and dried by N<sub>2</sub> gas. Finally, after standard RCA cleaning, the textured wafers were fabricated into solar cells using the standard process.

The morphology and structure of the samples were characterized by a Hitachi S-4800 scanning electron microscope (SEM). Hemispheric total reflectance for normal incidence was measured using a Varian Cary 5000 spectrophotometer equipped with an integrating sphere. The solar cell efficiency was measured using a BERGER Lichttechnik Single Cell Tester.

## 3. Results and discussions

### 3.1. Surface property of as-cut DWS and SWS wafers

The as-cut structure for the differently sawn wafers predetermines the texturization of the etched surface (Meinel et al., 2014). The surface morphology of the as-cut mc-Si wafers sliced with SWS and DWS method are shown in Fig. 1(a) and (b). The surface of the SWS mc-Si wafers shows randomly distributed microcracks and fractures due to a rolling-indenting model (Möller 2004; Wu, 2016) (Fig. 1(a)). However, the DWS mc-Si wafers show smooth parallel observed marks/grooves covering the surface that are sometimes interrupted by pits, leaving a rougher surface, as we can see in Fig. 1(b). These parallel grooves consisting of a slight range of 5 µm and high in a span of 650 µm, where the amorphous silicon has been identified by Raman analysis (Bidville

et al., 2009), enhance the visual appearance to the naked eyes, giving rise to a shiny surface for the DWS wafers. As a result, the initial reflectance of the DWS wafers is higher than that of the SWS wafers. However, the surface roughness for DWS wafers is 25% lower than that for SWS wafers (Chen et al., 2014), with the thicknesses of the saw-damage layers reduced by more than a factor of two compared to the SWS wafers (Watanabe et al., 2010). The diamond wire sawn technique is expected to become the mainstream wafering technology for the Si-based photovoltaic industry despite the existence of the amorphous silicon thanks to its huge contribution to the cost reduction of solar cells.

### 3.2. The orientation and optical property for different grains

In this part, the surface morphologies for sample A and sample B textured by CACE and HF/HNO<sub>3</sub> mixture solutions are shown in Fig. 1(c) and (d). We can observe from Fig. 1(d) that only some shallow pits exist on the surface of sample B, with most of the surface not textured any more, indicating that the HF/HNO<sub>3</sub> mixture solutions are not suitable for texturing DWS mc-Si wafers. In contrast, sample A was thoroughly textured with the CACE method; the surface structure is shown in Fig. 1(c). It is evident that the surface is covered by a series of inverted-pyramid-like structures and that the textured structures are different among the grains due to the orientation of the grains for mc-Si being inhomogeneously distributed and the anisotropic etching of CACE.

For the CACE technique, the reaction mechanism has been investigated in detailed in our previous work (Wang et al., 2015) and other studies (Peng et al., 2006a,b; Huang et al., 2011; Tian et al., 2007; Liu et al., 2012; Lu and Barron, 2013). In this case, the Cu-nano-particles population attached to c-Si is a function of the crystallographic plane orientation (Wang et al., 2015), resulting in anisotropic etching to form inverted pyramid structures on the Si <1 0 0> grains as well as IPL structures on the other grains, as shown in Fig. 3. Deep grooves are formed along the grain boundaries, as seen in Fig. 1(c) and (d). This outcome occurs because there are much more defects existing on the grain boundaries than inside the grains, accelerating the electron supply rates from the grain boundaries, resulting in a much higher etch rate.

Differently oriented grains give rise to different inverted-pyramid-like structures, which are covered by close-packed {1 1 1} crystal surfaces because of the anisotropic etching of CACE. During this etching process, the silicon atoms in the Si <1 0 0> are dissolved, making the {1 1 1} planes the surfaces. Here, the orientations of the different grains can be ensured by comparison of the SEM image with a theoretical calculation model that we have established for the first time. The schematics are shown in Fig. 2. To simply the model, the surface structure is described as the plane of a certain grain that incises the {1 1 1}-octahedron to form the final structure. For grains such as <11a>

whose planes intersect with the {1 1 1}-octahedron, one can expect four intersecting lines, with the isosceles-trapezoid formed shown in Fig. 2(a). The isosceles can be expressed by the following equations:

$$(1) \begin{cases} x + y + az = 1 \\ y - x + z = 1 \end{cases}, (2) \begin{cases} x + y + az = 1 \\ x - y + z = 1 \end{cases}.$$

According to these two equations, we can gain two vectors via assigning a value to each equation:

$$\vec{OA} = (a + 1/2, a - 1/2, -1), \vec{OB} = (a - 1/2, a + 1/2, -1).$$

We can choose the angle  $\theta$  between these two isosceles as the standard to determine the orientations of the grains. The  $\theta$  can be solved according to the trigonometric function:

$$\cos \theta = \frac{\vec{OA} \cdot \vec{OB}}{|\vec{OA}| \cdot |\vec{OB}|}.$$

Thereby,  $\theta$  is obtained according to the former formula for different grains; thus, offering a criterion for distinguishing between the grains. Additionally, the other angle  $\theta_e$ , existing in the structures formed during the etching process period, is easily gained by measurement (Fig. 2(b)). These two angles are uniform for the same grain, i.e.,  $\theta = \theta_e$ . If the  $\theta_e$  for a structure is consistent with the calculated result for the certain grain orientation, the orientation of the grain covered by this structure is then obtained. To demonstrate what we have proposed is reasonable, we carried out calculations for different grains. Take grain <1 1 2> as an example, with a value of 1 for “a” and  $\theta = 44.4^\circ$  for the theoretical calculation. As for the structure shown in Fig. 3(b), the  $\theta$  we measured using e-ruler is  $44.1^\circ$ , which is perfectly matched with the calculated result. In this way, we can determine the orientation of the grain to be <1 1 2> by measuring  $\theta$  for the texture structure shown in Fig. 3(b). In addition, we have determined the orientation of other grains according to our calculation model, with the results shown in Fig. 3. It is evident that there is a one-to-one correspondence between the grains and the final structures; thereby, we can distinguish the grains according to the final structures formed after CACE. For grain <1 1 3>, the structure close to the standard inverted pyramid is deeper than grain <1 1 2> and grain <1 1 0>, which one can expect to lead to a better light-trapping property. Details for light-trapping effects for different structures will be discussed later.

The surface optical properties for different grains are significantly changed following the anisotropic etching by CACE. The grains whose orientations are close to <1 0 0> form a standard inverted pyramid structure. Fig. 4(a) shows its cross-sectional image, where  $\alpha$  (the angle between the surface and slope) for a standard inverted pyramid is  $54.7^\circ$ , which has been confirmed in our previous work (Wang et al., 2015). For different grains, the reflectance is related to  $\alpha$ . When  $\alpha$  is greater than or equal to  $54.7^\circ$ , the normal incident light closed to the bottom of the structure will mostly undergo reflection three times, resulting in significant suppression for the light reflectance. When  $\alpha$  is between  $30^\circ$  and  $54^\circ$ , however, the normal incident light closed to the structure bottom will undergo reflection twice. The reflection will become only singular when  $\alpha$  is smaller than  $30^\circ$  due to the much shallower and flatter structure (Baker-Finch and McIntosh, 2010). To determine the relationship between  $\alpha$  and the orientations of different grains to further estimate the reflectance mechanisms and values, one new model, with  $\alpha = 90^\circ - \theta - \theta_1$ , is presented, with the graphics shown in Fig. 4(b). In this part, vector  $\vec{a}$  stands for the grain orientation <1 0 0> – the orientation for an inverted pyramid, rather than always being perpendicular to the wafer surface; the vector is on behalf of the orientations of grains <1 1 0> <1 1 3>, etc. In the relationship  $\alpha = 90^\circ - \theta - \theta_1$ ,  $\theta$  is the angle between  $\vec{a}$  and , which can be denoted as below:

$$\theta = \arccos \frac{\vec{a} \cdot \vec{b}}{|\vec{a}| \times |\vec{b}|}$$

$\theta_1$  is the angle between <1 0 0> and <1 1 1> and is  $36.3^\circ$ . With regard to different grains, the is known according to the model we have

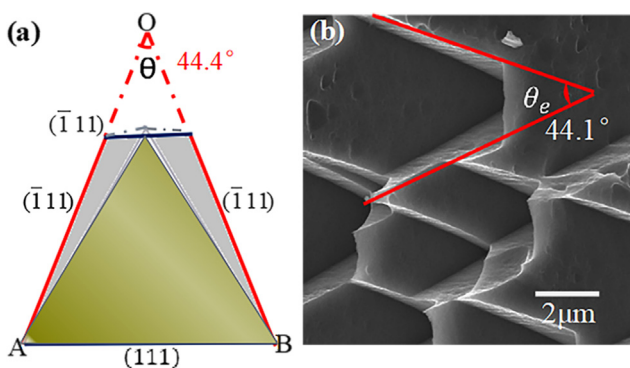


Fig. 2. The schematics used to calculate the orientation of grains: (a) the calculation model, (b) the experimental structure for grain <1 1 2>.

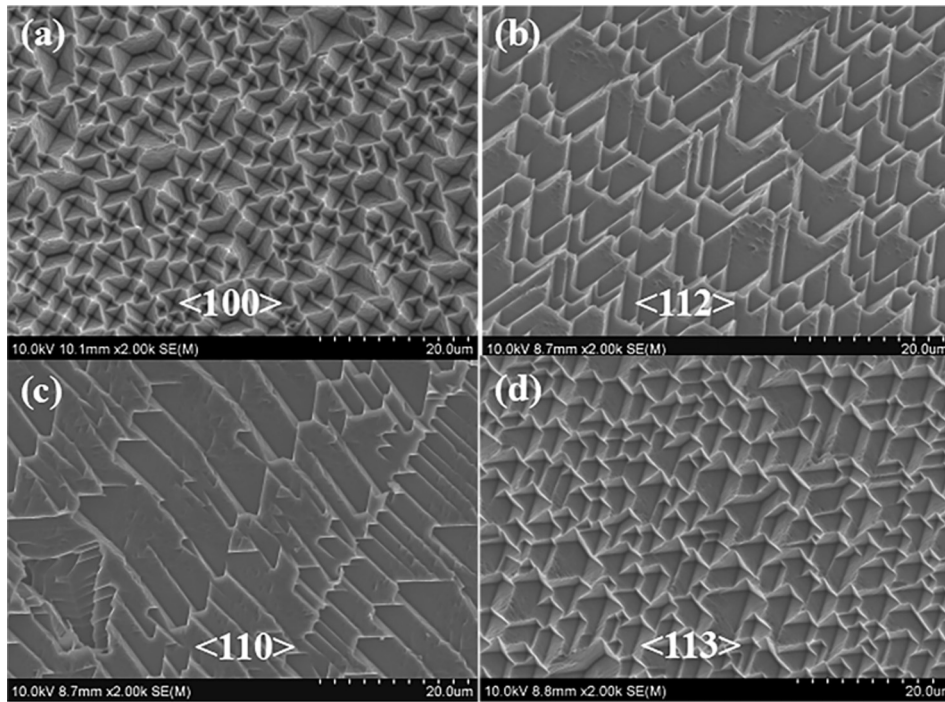


Fig. 3. The SEM top-view images of different grains for sample B; the grain orientations as shown in the figures were verified using the calculation model that we have established.

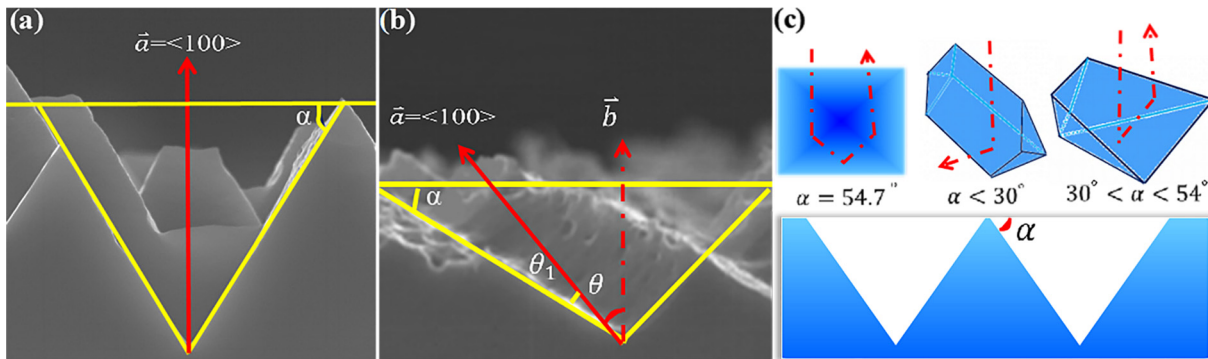


Fig. 4. (a), (b) The model used to confirm  $\alpha$  for the different grains and (c) the corresponding reflectance mechanisms for different  $\alpha$ . (a), (b) the cross-sectional images for grain  $\langle 100 \rangle$  and grain  $\langle 113 \rangle$ , respectively.

proposed above, as a consequence,  $\alpha$  for different grains can be gained on the basis of  $\alpha = 90^\circ - \theta - \theta_1$ , motivating one to understand the possible reflectance process and estimate the approximate reflectance value according to Fig. 4(c). Take grain  $\langle 113 \rangle$  for instance. The value obtained for  $\theta$  via calculation is  $23.5^\circ$ , so the  $\alpha$  for grain  $\langle 113 \rangle$  was determined through  $\alpha = 90^\circ - 35.3^\circ - 23.5^\circ$  is  $31.2^\circ$ , which is in accordance with the value of  $31^\circ$  for grain  $\langle 113 \rangle$  measured using e-ruler, as shown in Fig. 4(b). Therefore, we can conclude that the normal incident light near the structure bottom will mostly undergo reflection twice when incident onto the surface of grain  $\langle 113 \rangle$ , resulting in a reflectance value of approximately 20%. However, for grain  $\langle 110 \rangle$ ,  $\alpha$  is  $9.7^\circ$ , indicating a very flat structure and a much higher reflectance value of approximately 30% due to one-time reflection only occurring when normal incident light is incident onto the surface.

To further verify our models, we have carried out simulations and experiments, whose results are shown in Fig. 5. As seen from Fig. 5(a), (c) and (b), (d), it is clear that the simulation structures for grain  $\langle 113 \rangle$  and  $\langle 110 \rangle$  are almost the same as those realized during the CACE etching process. Importantly, we find from Fig. 5(e) that the reflectance spectra obtained for different grains using both simulations

with ray tracing and experimental measurements are in very good agreement with each other. For grain  $\langle 100 \rangle$ , the standard inverted pyramid structure formed with  $\alpha = 54.7^\circ$ , shows an excellent light-trapping property due to the triple bounce of the incident light, resulting in great suppression of the reflectance to a level as low as 8.8% (the red<sup>1</sup> line with filled circles shown in Fig. 5(c)). As for grain  $\langle 113 \rangle$ , the reflectance value is 20.8%, with  $\alpha = 31.2^\circ$ , indicating that the double bounce of light occurs near the structure bottom (red line with filled five-pointed stars shown in Fig. 5(c)). In addition, the  $\alpha$  is  $9.7^\circ$  for grains  $\langle 110 \rangle$ , implying that the normal incident light almost undergoes a one-time bounce due to the very flat structure, which leads to a high reflectance level of 31.7% (red line with filled triangles shown in Fig. 5(c)). The outcome obtained from simulations and verification work in concert with our previous discussion, which is sufficient proof to support our conclusions. Moreover, the two models that we have proposed for the first time provide better insights for the analysis of the

<sup>1</sup> For interpretation of color in Fig. 5, the reader is referred to the web version of this article.

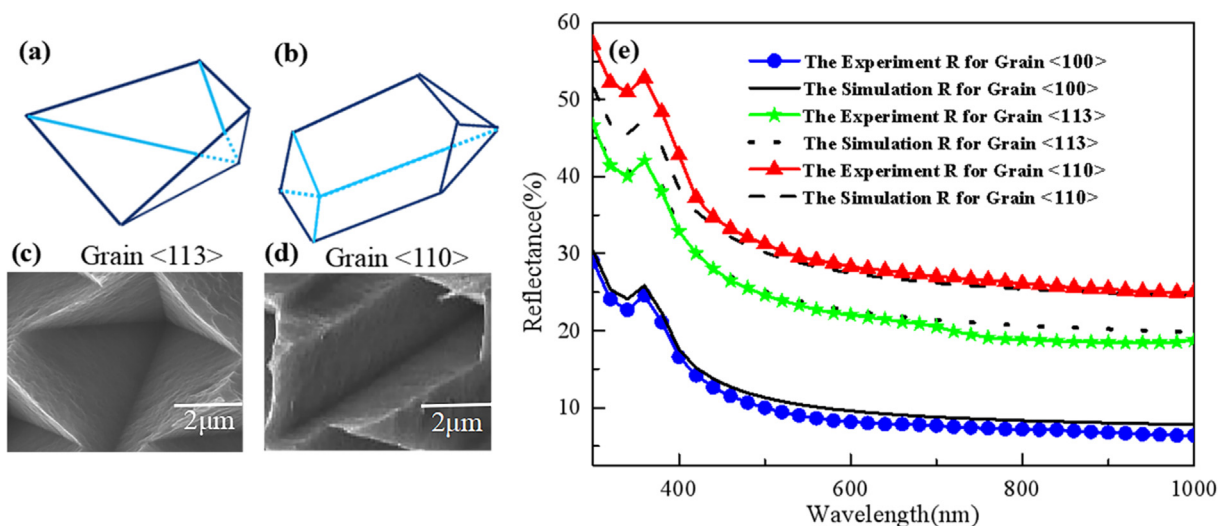


Fig. 5. The contrast between simulation results (a), (b) and experimental results (c), (d): (a), (c) for grain  $\langle 113 \rangle$ ; (b), (d) for grain  $\langle 110 \rangle$ . (e) is the reflectance obtained for different grains using different methods: the lines with and without symbols denote the experimental and simulation results (the solid line and the line with solid circle for grain  $\langle 100 \rangle$ , the short dash line and the line with solid star for grain  $\langle 113 \rangle$ , the long dash line and the line with solid triangle for grain  $\langle 110 \rangle$ ), respectively.

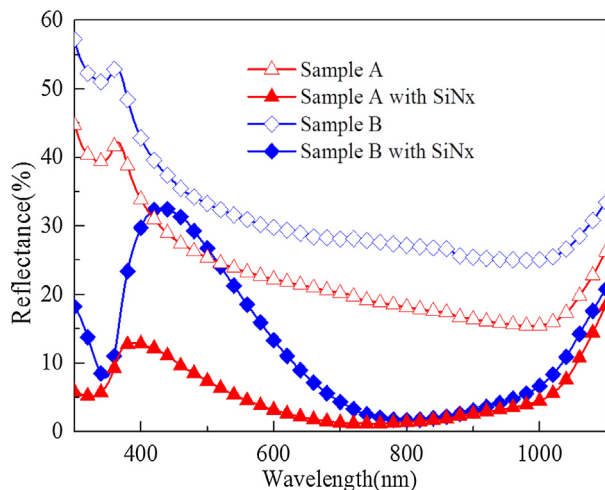


Fig. 6. The wafer-scale reflectance measured from 300 nm to 1100 nm for Sample A and Sample B as well as for samples with SiNx.

properties of mc-Si wafers textured by CACE.

The reflectance spectra measured over the wavelength range from 300 nm to 1100 nm for sample A and sample B before and after SiNx deposition are shown in Fig. 6. It should be noted that the reflectance for the mc-Si wafer-scale is a proximity-weighted average reflectance of all the grains. The main conclusion we have realized according to what we have shown in Figs. 4 and 5 is that grains such as grain  $\langle 100 \rangle$  and grain  $\langle 113 \rangle$  can greatly decrease the reflectance to a much lower level than that for as-cut wafers. Considering the small fraction of grains closed to the grains  $\langle 100 \rangle$ , the reflectance of the DWS mc-Si wafers cannot be reduced to a much lower level such as that for pyramid-textured mono-crystalline silicon wafers. As a result, the 22.4% reflectance of sample A is 8.4% lower than that for sample B (30.8%), and almost shows a single bounce when the normal incident light strikes the surface, as shown by the spectra in Fig. 6. More importantly, the reflectance for sample A was significantly suppressed to a much low level of 4.4% compared with sample B (13.1%) after SiNx deposition by PECVD. It is clear that the reflectance of the short-wavelength band for sample A with SiNx descends greatly in contrast with that for sample B, illustrating that the well textured front surface comprising IPL

structures dramatically increases the absorption of short-wavelength photons, which can greatly increase cell conversion efficiency.

### 3.3. The cell efficiency for wafers textured by CACE and acid etching

As mentioned above, the reflectance of DWS mc-Si wafers textured by CACE was greatly decreased and can facilitate the performance of solar cells. To verify the feasibility of this technique, sample A and sample B wafers were fabricated into solar cells using the current production line suited for SWS mc-Si.

The best and average cell parameters measured by a BERGER Lichttechnik Single Cell Tester for sample A and sample B are listed in Table 1. It is clear that sample A shows a much higher cell efficiency of approximately 19.33%, as well as a higher  $J_{sc}$  of 37.42 mA/cm<sup>2</sup>, compared to sample B, which shows values of 18.83% and 36.69 mA/cm<sup>2</sup>, respectively. The reason for the higher  $J_{sc}$  is mainly due to the low reflectance and high light absorption because of the IPL structures, which further enhance the cell efficiency, indicating that our technique has a much more pronounced edge for texturing DWS mc-Si wafers compared to the use of HF/HNO<sub>3</sub> mixture solutions. In addition, one can observe an evident scatter in  $U_{oc}$  and FF among these two group samples, with the higher  $U_{oc}$  and FF not only increasing the cell efficiency but also greatly reducing the module loss. The higher  $J_{sc}$ , together with the higher FF and  $U_{oc}$ , make the average cell efficiency for sample A is 0.52% higher than that for sample B. On the other hand, the higher  $U_{oc}$  for sample A interprets that the IPL structure is good at passivation and decreasing the carrier recombination. In addition, much more effort is required due to the limitation of our experiment conditions as well as the parameters on the production line suited for SWS wafers are not that well matched with our texture technique of DWS wafers. Therefore, the cell conversion efficiency is expected to be

Table 1

A summary of the best and average solar cell efficiencies obtained for sample A and sample B.

Sample	$U_{oc}$ (mV)	$J_{sc}$ (mA/cm <sup>2</sup> )	FF (%)	Eff (%)	
Sample A	640.3	37.42	80.67	19.33	Best
	637.2	37.12	80.48	19.03	Average
Sample B	638.1	36.69	80.44	18.83	Best
	636.0	36.25	80.28	18.51	Average

greatly improved following further optimization. This study is a successful attempt to apply the CACE technique for texturing DWS mc-Si wafers with inverted pyramid structures to greatly enhance the performance of DWS mc-Si solar cells.

#### 4. Conclusions

In summary, we have proposed an efficient method for thoroughly texturing DWS mc-Si wafers by using Cu-assisted chemical etching (CACE). This texture includes a series of inverted-pyramid-like structures on the surface that are very effective for significantly reducing light reflectance and improving Jsc. The cell efficiency was dramatically enhanced. The average cell efficiency with high Jsc and high FF resulting from use of the CACE technique is 0.52% higher than that obtained for conventionally textured solar cells. In addition, we have established new models to confirm the orientations of grains and their reflectance properties according to the structures formed during the CACE process, which provides better insights for analyzing the properties of DWS mc-Si wafers textured by CACE. Moreover, our simple and low-cost technique is comparable with the current production line, demonstrating great potential to become a standard process for mass manufacture of highly efficient DWS mc-Si solar cells.

#### Acknowledgements

This work was supported by the National Science Foundation of China (Grant Nos. 11675280 and 11674405) and Science and Technology Department of Jiangsu Province (Technological Achievements Transformation Project, Grant Nos. BA2017137).

#### References

- Baker-Finch, S.C., McIntosh, K.R., 2010. Reflection of normally incident light from silicon solar cells with pyramidal texture. *Prog. Photovolt: Res. Appl.* 19 (4), 406–416.
- Bhagavat, M., Prasad, V., Kao, I., 2000. ElastoHydrodynamic interaction in the free abrasive wafer slicing using a wiresaw: modeling and finite element analysis. *J. Tribol.* 122, 394–404.
- Bidville A., et al., 2009. Diamond wire-sawn silicon wafers-from the lab to the cell production. In: *Proceedings of the 24th EU PV-SEC.* 1400–1405.
- Cao, F., et al., 2015. Next-generation multi-crystalline silicon solar cells: diamond-wire sawing, nano-texture and high efficiency. *Sol. Energy Mater. Sol. Cells* 141, 132–138.
- Chen, W.H., et al., 2014. On the nature and removal of saw marks on diamond wire sawn multicrystalline silicon wafers. *Mater. Sci. Semicond. Process* 27, 220–227.
- Chen, K.X., et al., 2015. Novel texturing process for diamond-wire-sawn single-crystalline silicon solar cell. *Sol. Energy Mater. Sol. Cells* 133, 148–155.
- Chung, C., Nhat, L.V., 2014. Generation of diamond wire sliced wafer surface based on the distribution of diamond grits. *Int. J. Precis. Eng. Man.* 15, 789–796.
- De Wolf S., et al., 2000. Towards industrial application of isotropic texturing for multi-crystalline silicon solar cells. in: *Proceedings of the Sixteenth European Photovoltaic Solar Energy Conference, Glasgow, UK.*, 521–1523.
- Fashina, A.A., et al., 2015. Surface texture and optical properties of crystalline silicon substrates. *J. Renew. Sustain. Energy* 7 (6), 063–119.
- Huang, Z.P., et al., 2011. Metal-assisted chemical etching of silicon: a review. *Adv. Mater.* 23, 285–308.
- Kawasegi, N., et al., 2005. Etch stop of silicon surface induced by tribo-nanolithography. *Nanotechnology* 16, 1411–1414.
- Kumagai, A., 2015. Texturization using metal catalyst wet chemical etching for multi-crystalline diamond wire sawn wafer. *Sol. Energy Mater. Sol. Cells* 133, 216–222.
- Lippold, M., et al., 2014. Texturing of SiC-slurry and diamond wire sawn silicon wafers by HF–HNO<sub>3</sub>–H<sub>2</sub>SO<sub>4</sub> mixtures. *Sol. Energy Mater. Sol. Cells* 127, 104–110.
- Liu, Y.P., et al., 2012. Nanostructure formation and passivation of large-area black silicon for solar cell applications. *Small* 8, 1392–1397.
- Lu, Y.T., Barron, A.R., 2013. Nanopore-type black silicon anti-reflection layers fabricated by a one-step silver-assisted chemical etching. *Phys. Chem. Chem. Phys.* 15 (24), 9862–9870.
- Macdonald, D.H., et al., 2004. Texturing industrial multicrystalline silicon solar cells. *Sol. Energy* 76 (1–3), 277–283.
- Meinel, B., et al., 2014b. Comparison of diamond wire cut and silicon carbide slurry processed silicon wafer surfaces after acidic texturization. *Mater. Sci. Semicond. Process.* 26, 93–100.
- Meinel, B., et al., 2014a. Comparison of diamond wire cut and silicon carbide slurry processed silicon wafer surfaces after acidic texturization. *Mater. Sci. Semicond. Process.* 26, 93–100.
- Meinel, B., Koschwitz, T., Acker, J., 2012. Textural development of SiC and diamond wire sawed sc-silicon wafer. *Energy Procedia* 27, 330–336.
- Meng, C.H., Zhou, L., 2014. Mechanical behavior of diamond-sawn multi-crystalline silicon wafers and its improvement. *Silicon* 6, 129–135.
- Möller, H.J., 2004. Basic mechanisms and models of multi-wire sawing. *Adv. Eng. Mater.* 6, 501–513.
- Möller, H.J., et al., 2005. Multicrystalline silicon for solar cells. *Thin Solid Films* 487, 179–187.
- Möller, H.J., 2006. Wafering of silicon crystals. *Phys. Status Solidi A* 203, 659–669.
- Möller, H.J., et al., 2011. Growth optimization of multicrystalline silicon. *Energy Procedia* 3, 2–12.
- Peng, K.Q., et al., 2006a. Metal-particle-induced, highly localized site-specific etching of Si and formation of single-crystalline Si nanowires in aqueous fluoride solution. *Chem.-Eur. J.* 12, 7942–7947.
- Peng, K.Q., et al., 2006b. Fabrication of single-crystalline silicon nanowires by scratching a silicon surface with catalytic metal particles. *Adv. Funct. Mater.* 16, 387–394.
- Tian, B.Z., et al., 2007. Coaxial silicon nanowires as solar cells and nanoelectronic power sources. *Nature* 449, 885–888.
- Wang, Y., et al., 2015. Maskless inverted pyramid texturization of silicon. *Sci. Rep-UK* 5, 10843.
- Watanabe, N., et al., 2010. Characterization of polycrystalline silicon wafers for solar cells sliced with novel fixed-abrasive wire. *Prog. Photovolt: Res. Appl.* 18, 485–490.
- Wu, C., et al., 2001. Near-unity below-band-gap absorption by microstructured silicon. *Appl. Phys. Lett.* 78, 1850.
- Wu, H., 2016. Wire sawing technology: a state-of-the-art review. *Precis. Eng.* 43, 1–9.
- Yang, C., et al., 2013. Comparative analysis of fracture strength of slurry and diamond wire sawn multicrystalline silicon solar wafers. *Adv. Eng. Mater.* 15, 358–365.
- Yu, X.G., et al., 2012. Thin Czochralski silicon solar cells based on diamond wire sawing technology. *Sol. Energy Mater. Sol. Cells* 98, 337–342.